Energy Engineering

Tech Science Press

https://doi.org/10.32604/ee.2026.078939

ARTICLE

# Design of Anti-Condensation System for Tower Solar Thermal Power Plant Coupled with Heat Pumps

**Kai Li[1], Yongheng Zhang[2,*], Kai Sun[1] and Mingkuan Rong[3]**

[1]School of Mechatronic Engineering, Lanzhou Jiaotong University, Lanzhou, China
[2]School of New Energy and Power Engineering, Lanzhou Jiaotong University, Lanzhou, China
[3]Luneng New Energy (Group) Gansu Branch, China Green Development Investment Group, Lanzhou, China

*Corresponding Author: Yongheng Zhang. Email: zhangyh@mail.lzjtu.cn

Received: 11 January 2026; Accepted: 13 April 2026; Published: 30 August 2026

**ABSTRACT:** This study designs a supercritical $CO_2$ heat pump anti-condensation system for a 50 MW tower solar thermal power plant in northwest China to prevent molten salt solidification in pipelines and storage tanks. A thermodynamic model is established to analyze the effects of key parameters (heat release power, maximum/minimum cycle pressure, heat source temperature, and isentropic efficiency) on the coefficient of performance (COP), with the simulation model validated against literature experimental data. Heat dissipation loss of the low-temperature molten salt tank is calculated to determine system capacity, and an economic comparison is conducted among the proposed heat pump, electric tracing, coal-fired boiler, and gas boiler. Results indicate that COP increases with higher heat release power, heat source temperature, and isentropic efficiency, but decreases with rising maximum cycle pressure. The minimum cycle pressure shows a non-monotonic effect due to density variations near the critical point. The heat pump system achieves a round-trip thermal efficiency of 35%–40%, and its annual operating cost is lower than conventional anti-condensation methods, offering a clean and economically viable solution for molten salt freeze protection.

**KEYWORDS:** Heat pump; supercritical carbon dioxide; freeze protection; coefficient of performance (COP); heat loss calculation

## 1 Introduction

Molten salt dual-tank storage technology is widely used in concentrating solar thermal power (CSP) plants [1]. A typical tower-type solar thermal power station generally uses binary molten salt (60% $NaNO_3$, 40% $KNO_3$) as the heat transfer medium for its energy storage and heat exchange subsystems. To avoid system failure, molten salt is not allowed to solidify under any conditions. A commonly adopted anti-condensation measure is to use a molten salt low-temperature heat storage tank to maintain low-speed pipeline circulation at night or on cloudy days to maintain the system temperature. To maintain the minimum operating temperature of the low-temperature thermal storage tank (260°C), it is usually necessary to install electric heat tracing systems or gas-fired or coal-fired boilers on the pipelines and thermal storage tanks [2].

Kearney et al. (2004) proposed that molten salt in the low-temperature thermal storage tank maintains low-speed circulation in pipelines at night or on cloudy days to maintain the system temperature can be chosen as a method of anti-condensation in power plant [3]. In the research on thermoelectric energy storage and waste heat utilization, high-temperature heat pumps have made certain progress in improving energy quality by using circulating water as a source. In recent years, heat pump technology using $CO_2$ as the working fluid has developed rapidly [4]. Chamoun established a new simulation system for twin-screw compressors and built an experimental platform. The coolant fluid exhibited high performance in the temperature range of 130°C–140°C [5,6]. Morandin et al. studied the influence of various thermodynamic parameters of carbon dioxide working fluid on the overall efficiency of the system during in the cycle [7].

Zhang et al. developed a multiple renewable energy complementary heat pump system integrating and experimentally demonstrated in Lanzhou that under three operating modes, the system achieved average COP ranging from 1.70 to 2.32, with the proportion of air heat input decreasing significantly when solar or biomass energy was introduced [8]. Li et al. proposed a solar polygeneration system integrating an absorption heat pump and a humidification-dehumidification desalination unit based on a 1 MW tower plant in Beijing; dynamic simulation results showed that the system achieved a heat pump COP of 1.39–1.73, increased fresh water production with GOR from 2.48 to 2.67, and raised the maximum power generation efficiency from 18.66% to 19.22% compared with the original plant [9]. Addressing the dual challenges of environmental degradation and sustainable development, Shaik et al. proposed a polygeneration system that integrates a solar-powered heat pump/vapor-compression refrigeration cycle with a humidification–dehumidification desalination unit, recovering waste heat from the condenser to produce cooling, hot water, and fresh water, and evaluated the effects of key parameters on the system's thermodynamic and exergy performance [10].

In this article, a design of a heat pump anti-condensation system based on the inverse Brayton cycle is carried out. Referring to pumped thermal electricity storage (PTES), the molten salt in the low-temperature heat storage tank is heated by a heat pump and its temperature is designed to be higher than the anti-condensation temperature. A heat pump system is established to analyze influencing factors of COP, and the heat loss calculations in engineering applications is carried out based on the simulation model. This article also analyzes the economy of supercritical $CO_2$ heat pumps.

## 2 Experimental System Modeling and Optimization

### *2.1 Experimental System Parameters and Modeling*

A typical tower solar thermal power generation system is shown in Fig. 1, which can be divided into three subsystems according to composition, concentrated heat collection subsystem, energy storage & heat exchange subsystem, and power cycle subsystem.

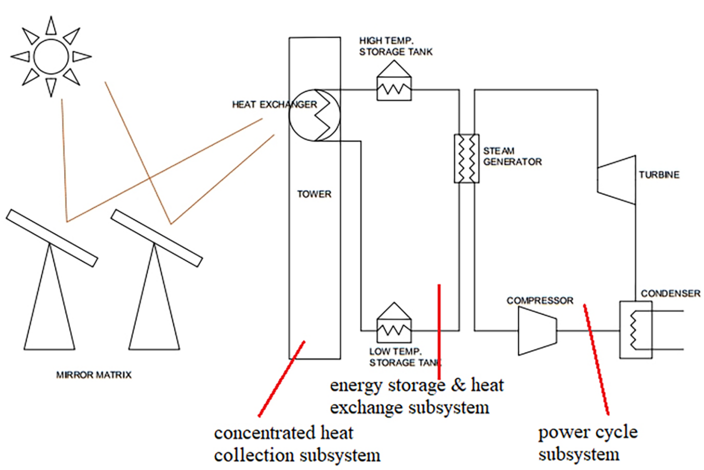


**Figure 1:** Schematic diagram of tower solar thermal power plant system.

As shown in Fig. 2, the heat pump uses a motor as a compressor, enabling the circulating coolant to absorb heat from a low-temperature heat source (the coolant of the power cycle subsystem) and release heat to a high-temperature heat source (the low-temperature heat storage tank), thereby converting electrical energy into thermal energy to maintain the temperature of the heat storage medium in the tank. The cooling water passing through the cooler serves as the low-temperature heat source for the heat pump, while the low-temperature molten salt heat storage tank acts as the system's high-temperature heat source.

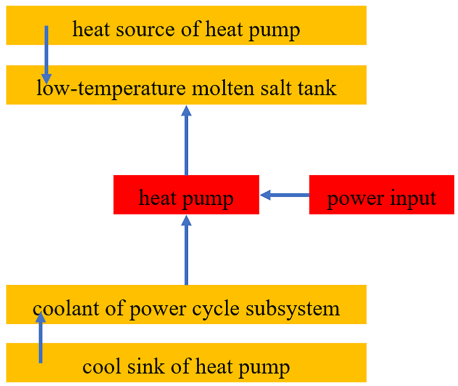


**Figure 2:** Schematic diagram of heat pump anti-condensation system.

Heat pump system uses supercritical carbon dioxide (S-$CO_2$) as circulating coolant for the heat pump anti-condensation system, as shown in Fig. 3. The cool source of the heat pump is the circulating water of the power cycle subsystem, and the heat source is the molten salt in low-temperature tank.

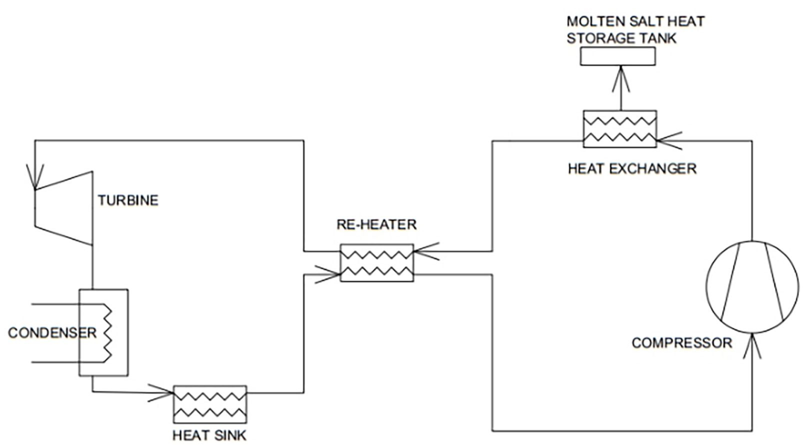


**Figure 3:** Schematic diagram of anti-condensation system for S-$CO_2$ heat pumps.

The temperature-entropy diagram of the heat pump energy storage system is shown in Fig. 4. The main process is as follows: the working fluid enters a motor-driven compressor and is compressed from a medium-temperature, low-pressure state to a high-temperature, high-pressure state; the working fluid releases heat in the high-temperature heat exchanger, transitioning to a medium-low-temperature, high-pressure state, while the molten salt in the heat storage tank absorbs the heat released by the working fluid; the working fluid releases heat at the hot side of the recuperator to the cold side of the recuperator, resulting in a temperature decrease; the working fluid undergoes isentropic expansion and isobaric heat release through the turbine and cooler, reducing its temperature and pressure to a certain state; after absorbing heat from the heat exchanger coupled with the low-temperature heat source, the working fluid receives heat released from the hot side at the cold side of the recuperator, returning to its initial medium-temperature state before the cycle begins, thus completing the cycle.

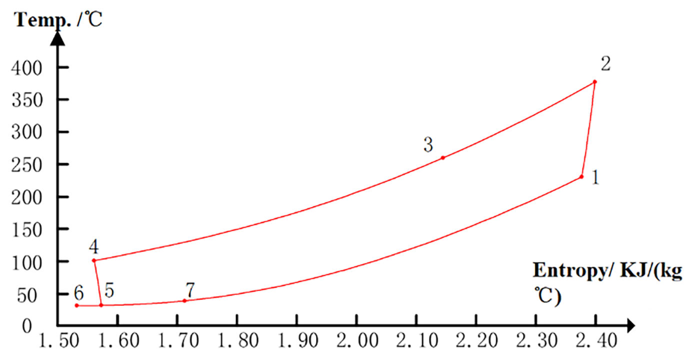


**Figure 4:** T-s diagram of heat pump system.

The details of heat pump system can be found in Table 1. This research established on a 50 MW concentrated solar power plant in northwest China, using binary molten salt as coolant. Simulation of experimental system is conducted by using MATLAB, and the physical characteristics of all coolant are obtained through REFPROP (Reference Fluid Properties), a software developed by the US National Institute of Standards and Technology (NIST).

**Table 1:** System boundary conditions.

| Parameters | Value |
|---|---|
| Coolant | $CO_2$ (R744) |
| Heat storage | Binary molten salt |
| Compressor variable efficiency | 90% |
| Turbine variable efficiency | 90% |
| Maximum system temperature (°C) | 290 |
| Minimum system temperature (°C) | 32 |
| Temperature difference of heat exchanger (°C) | 5 |
| Compressor inlet temperature (°C) | 230 |
| Compressor inlet pressure (MPa) | 7.3 |
| Mass of storage medium (t) | 15,000 |

Simulation model design relies on the following fundamental assumptions: Energy exchange of the system with external factors is disregarded during heat transmission. No energy loss occurs during the energy exchange of coolant within the heat exchanger and regenerator. The system is assumed to be free from drag and mechanical losses. Pressure drops in heat exchangers and pipelines are negligible.

### *2.2 Numerical Simulation*

#### *2.2.1 Model Setup*

The supercritical system of $CO_2$ heat pump is established based on the parameters and hypotheses outlined in Section 2.1. In Fig. 4, the process from Node 1 to Node 2 involves the compression process of compressor. The specific enthalpy under isentropic compression at Node 2, is given by

$$s_1 = f\_s_1 (T_1, p_1) \tag{1}$$

$$h_{2s} = f\_h_{2s} (s_1, p_2) \tag{2}$$

The process from Node 2 to Node 3 signifies the exothermic process from system into the cryogenic heat storage tank, and thermodynamic properties at these nodes are derivable through the formulas:

$$p_2 = p_3 \tag{3}$$

$$h_2 = h_1 + (h_{2s} - h_1) / \eta_s \tag{4}$$

$$T_2, s_2, p_2 = f_{\_T_2, s_2, p_2} (h_2, p_3) \tag{5}$$

Utilizing the characteristics of S-$CO_2$, the cooling temperature of the system is derived by

$$h_3, s_3, p_3 = f_{\_h_3, s_3, p_3} (T_3) \tag{6}$$

From Node 3 to Node 4, a reheat process occurs with a 5°C subcooling for the reheater, and the process from Node 2 to Node 3 corresponds to the enthalpy change from Node 6 to Node 1:

$$h_4, s_4 = f_{\_h_4, s_4} (T_3 - 5, p_3) \tag{7}$$

$$m_1 (h_3 - h_2) = m_2 (h_6 - h_1) \tag{8}$$

From Nodes 4 to 5, an isentropic expansion occurs, and the thermodynamic properties of Node 5 are expressed as:

$$s_4 = s_5 \tag{9}$$

$$T_5, s_5 = f_{\_T_5, s_5} (h_4, p_3) \tag{10}$$

Based on the properties of S-$CO_2$, the cooling temperature of the system is obtained by

$$h_6, s_6, p_6 = f_{\_h_6, s_6, p_6} (T_6) \tag{11}$$

Then, the work done by the compressor is

$$w = \frac{1}{\eta_m} (h_2 - h_1) \tag{12}$$

$$C_{cop} = \frac{h_3 - h_2}{w} \tag{13}$$

*2.2.2 Validation of Numerical Models*

This study employs experiment data of Salomone-González et al. (2020) for verification of the heat pump model [11]. The system utilizes argon as the circulating fluid, while binary salt mixture (60% $NaNO_3$, 40% $KNO_3$) serves as the heat source and methanol acts as the cooling source. The simulation results, presented in Table 2, demonstrate a satisfactory agreement with prior research.

**Table 2:** Comparison of heat pump model validation.

| Temp. at Different Points | Experiment Data of Salomone, 2020 | Simulation Results |
|---|---|---|
| Inlet temp. of heat source (°C) | 544 | 544 |
| Outlet temp. of heat source (°C) | 857.5 | 855.04 |
| Inlet temp. of cooling source (°C) | 300 | 300 |
| Outlet temp. of cooling source (°C) | 281.7 | 281.96 |
| Inlet temp. of compressor (°C) | 294.2 | 293.58 |
| Outlet temp. of compressor (°C) | 862.2 | 862.2 |
| Inlet temp. of expander (°C) | 560.8 | 569.42 |
| Outlet temp. of expander (°C) | 241.9 | 241.9 |
| Coefficient of performance (COP) | 1.20 | 1.19 |

*2.2.3 Numerical Result and Analysis*

The coefficient of performance (COP) serves as the key metric for evaluating the efficiency of a heat pump system, and this study aims to maximize its value. Optimizing the COP typically involves adjusting several thermodynamic parameters, including the system's heat release power, maximum and minimum cycle pressures, heat source temperature, and isentropic efficiency [12]. In this work, a detailed analysis is conducted to examine the individual impact of each of these parameters on the overall system COP.

(1) Analysis of disturbance parameters of system heat release power

Fig. 5 illustrates the correlation between heat pump COP and exothermic power within the cycle. Increasing in exothermic power indicates that the system has access to a more effective cold source with a lower temperature, which is beneficial for improving the COP. With the S-$CO_2$ cycle parameters steady, the compression power consumption stays nearly constant. Concurrently, as the molten salt's exothermic power augments, the turbine's inlet temperature of S-$CO_2$ decreases, causing a decline in turbine output power. This leads to a much lower increase in net compression power consumption than the increase in heat release power of the molten salt, thus gradually increasing the system COP. With an increased circulating water flow rate, the inlet temperature of S-$CO_2$ on low-temperature side rises, subsequently raising the outlet temperature on high-temperature side. Consequently, the turbine output power increments, while compression power consumption and molten salt exothermic power stay constant. Simulation results reveal that at a fluid flow rate of 8 kg/s, when the exothermic power increases from 700 to 900 MW, the COP increases from 1.11 to 1.36.

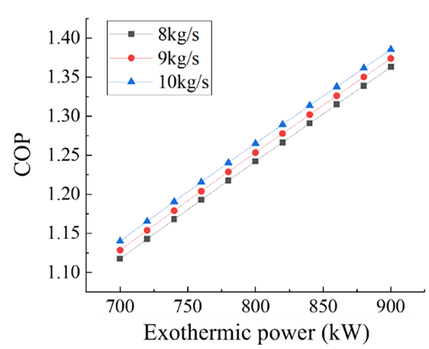


**Figure 5:** COP vs. system exothermic power curve.

(2) Analysis of disturbance parameters of maximum cycle pressure

The relationship curve between heat pump COP and maximum cycle pressure is shown in Fig. 6. When other cycle parameters of S-$CO_2$ are constant, as the maximum cycle pressure increases, the compression power consumption during the heat pump cycle increases gradually. As the heat release power to the molten salt remains constant, although both the inlet turbine temperature and pressure of the S-$CO_2$ increase, resulting in a gradual increase in the output power of the turbine, the increase is relatively small, which leads to an increase in the net compression power consumption of the cycle. Therefore, the COP of the heat pump system gradually decreases. As the mass flow rate of the circulating control molten salt in the heat exchanger remains constant, with the temperature of the heat exchanger gradually increasing, the heat absorption capacity of the molten salt gradually increases. Then with the outlet temperature of the molten salt increasing, the COP gradually increases. According to the calculation results, when the molten salt temperature is 290°C and the maximum cyclic pressure increases from 25 to 30 MPa, COP decreases from 1.38 to 1.21.

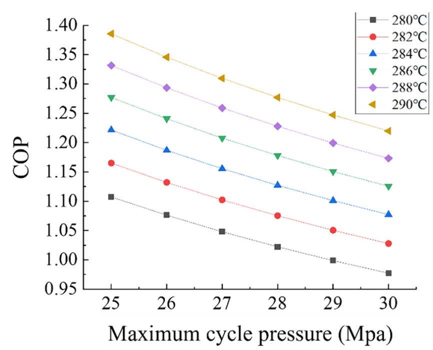


**Figure 6:** COP vs. maximum cycle pressure curve.

(3) Analysis of disturbance parameters of minimum cycle pressure

The relationship curve between heat pump COP and maximum cycle pressure is shown in Fig. 7. The COP decreases at first and then increases, which is due to the drastic density changes of S-$CO_2$ near the critical point. The density near the critical point is higher, while the density away from the critical point is lower. The energy consumption of the compressor increases, making the COP decreases consequently. According to the calculation results, when the molten salt temperature is 263°C, the COP changes from 1.38 to 1.36 as the minimum cyclic pressure is increased from 7.5 to 8.0 MPa.

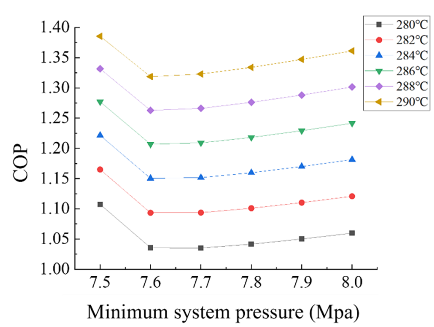


**Figure 7:** COP vs. minimum system pressure curve.

(4) Analysis of disturbance parameters of heat source temperature

As shown in Fig. 8, there is a linear relationship between heat pump COP and molten salt outlet temperature. When the inlet temperature of the molten salt is constant, to maintain energy balance, changes in the outlet temperature of the molten salt will cause the changes in the outlet temperature of the circulating working fluid side, the heat generated by the heat exchanger, and the work done by the expander. Thereby leading to the same trend of the system COP. According to the calculation results, the COP of the heat pump increases with the increase of the inlet temperature of the molten salt. Under the condition of a circulating pressure of 25 MPa, when the inlet temperature of the molten salt increases from 280°C to 390°C, the COP increases from 1.10 to 1.38.

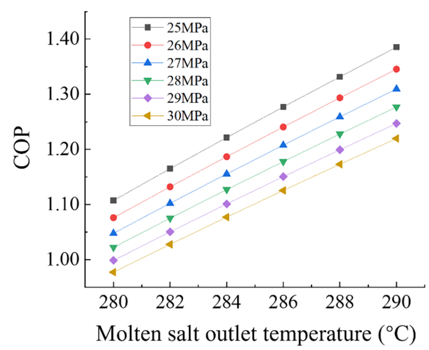


**Figure 8:** COP vs. heat source temperature curve.

(5) Analysis of disturbance parameters of isentropic efficiency of compressor/expander

The relationship curve between COP of heat pump and isentropic efficiency of compressor or expander is shown in Fig. 9. The operation of compressors and expanders is generally a variable process. As the isentropic efficiency of the compression or expansion process changes, the power consumption of the compressor and expander will change accordingly, leading to a similar tendency in the COP of the entire system. As illustrated in Fig. 9, a direct correlation can be observed between the COP of the heat pump and the rising isentropic efficiency. Quantitative analysis reveals that when the isentropic efficiency of the compressor or expander advances from 0.80 to 0.95 at a constant molten salt temperature of 390°C, a substantial rise in COP occurs, going from 1.18 to 1.49.

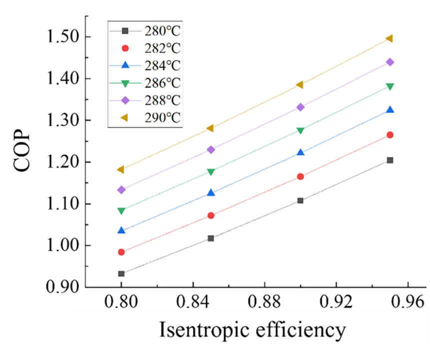


**Figure 9:** COP vs. compressor/expander isentropic efficiency curve.

## 3 Economic Benefit Analysis

To confirm the capacity of the anti-condensation heat pump, it is necessary to calculate the heat dissipation power of the heat storage tank. The molten salt heat storage tank of the solar thermal power plant can be simplified into a vertical cylindrical tank, and the tank body can be divided into three parts: the tank bottom, the top, and the wall. The heat exchange between the tank and the outside is mainly conducted in two forms: radiation and convection. The temperature of the air inside the tank and above the molten salt can be considered equivalent to the temperature of the molten salt, so in this article, the height of the molten salt liquid level inside the tank is not considered [13].

### *3.1 Setup and Validation of Numerical Low-Temperature Molten Salt Tank Models*

#### *3.1.1 Calculation of Total Heat Transfer Coefficient and Total Heat Loss*

The total heat transfer coefficient $h$ is the sum of the radiative heat transfer coefficient $h_r$ and the convective heat transfer coefficient $h_c$.

$$h = h_r + h_c \tag{14}$$

According to the law of conservation of energy, the total heat loss is obtained by analyzing the wall, top, and bottom of the heat storage tank,

$$Q_{loss} = A\left(T_{inner} - T_a\right) / \left(\frac{1}{h} + \frac{\delta_1}{\lambda_1}\right) \tag{15}$$

#### *3.1.2 Calculation of Radiative Heat Transfer Coefficient*

The radiative heat transfer coefficient can be expressed as:

$$h_r = 4\sigma\varepsilon\left(\frac{T_{outer} + T_a}{2}\right)^3\left(1 + \frac{T_{outer} - T_a}{T_{outer} + T_a}\right) \tag{16}$$

The radiation heat transferred inside the tank is mainly between the molten salt, the air inside the tank, and the wall surface of the heat storage tank, which can be expressed as:

$$Q_1 = \sigma\left(T_{sur}^5 - T_{top}^5\right) / \left(\frac{1-\varepsilon_{sur}}{\varepsilon_{sur}A_{sur}} + \frac{1}{A_{top}X_{top,sur}} + \frac{1-\varepsilon_{top}}{\varepsilon_{top}A_{top}}\right) \tag{17}$$

$$Q_2 = \sigma\left(T_{sur}^5 - T_S^5\right) / \left(\frac{1-\varepsilon_{sur}}{\varepsilon_{sur}A_{sur}} + \frac{1}{A_{S2}X_{S2,sur}} + \frac{1-\varepsilon_S}{\varepsilon_S A_{S2}}\right) \tag{18}$$

The angle coefficient between the surface of molten salt and the top of the tank is expressed as [14]:

$$X_{sur,top} = \frac{1}{2}\left(1 + \frac{1+\left(r_2/d\right)_2^2}{\left(r_1/d\right)^2}\right) - \frac{1}{2}\left(\left(1 + \frac{1+\left(r_2/d\right)^2}{\left(r_1/d\right)^2}\right)^2 - 4\left(\frac{r_1}{r_2}\right)^2\right)^{\frac{1}{2}} \tag{19}$$

#### *3.1.3 Calculation of Convective Heat Transfer Coefficient*

The convective heat transfer coefficients of molten salt and air with various surfaces follow Newton's cooling formula

$$Q_{cv,loss} = Ah_c\Delta T \tag{20}$$

(1) The convective heat transfer coefficient on the bottom surface of a heat storage tank is expressed as:

$$Nu = 0.27\left(GrPr\right)^{1/4}, 10^{5} < GrPr < 10^{10} \tag{21}$$

(2) When the gas temperature inside the heat storage tank is higher than the temperature of the molten salt, the convective heat transfer coefficient can be expressed as:

$$Nu = 0.27\left(GrPr\right)^{1/4}, 10^{5} < GrPr < 10^{6} \tag{22}$$

Conversely, when the gas temperature inside the heat storage tank is higher than the temperature of the molten salt, the convective heat transfer coefficient can be derived by:

$$Nu = 0.54\left(GrPr\right)^{1/4}, 10^{4} < GrPr_{r} < 10^{7} \tag{23}$$

$$N_{u} = 0.15\left(G_{r}P_{r}\right)^{1/4}, 10^{7} < G_{r}P_{r} < 10^{11} \tag{24}$$

When convective heat transfer occurs between molten salt and the lower part of the heat storage tank wall, the convective heat transfer coefficient is obtained according to:

$$N_{u} = \frac{0.68{R_{a}}^{1/4}{G_{r}}^{1/4}}{\left[0.952 + P_{r}\right]^{1/4}}, 10 < G_{r}P_{r} < 10^{8} \tag{25}$$

$$Nu = 0.13\left(GrPr\right)^{1/3}, GrPr > 10^{9} \tag{26}$$

### *3.2 Validation of Heat Transfer Model and Heat Dissipation Calculation*

To verify the accuracy and reliability of the heat transfer model for the low-temperature molten salt storage tank in Section 3.1, in this study, two heat storage tanks from the Solar Two power plant in the United States are selected for analysis [15]. Galerkin method [16] is adopted to solve the heat dissipation power of the low-temperature and high-temperature molten salt storage tank through Fluent. According to the results in Table 3, the error between the numerical model and the actual data is less than 3%, indicating that the model works well [17].

**Table 3:** Comparison of experimental data and simulated values of energy loss in molten salt heat storage tanks.

| Data | Loss of Low-Temperature Tank/kW | Loss of High-Temperature Tank/kW |
|---|---|---|
| Experiment data of Solar Two power plant | 44 ± 6.6 | 102 ± 21 |
| Simulation result | 43.85 | 99.55 |

The parameters of a 50 MW tower solar thermal power plant equipped with a molten salt heat storage tank are shown in Table 4. The tank body is made of carbon steel plate and contains an insulation layer made of 3 m-thick mineral wool inside. In addition to the mineral wool, a 3 m-thick refractory brick is added to the bottom of the tank. The design ambient temperature is taken as the average winter temperature of −8°C, and the wind speed is taken as the annual average wind speed of 2.5 m/s.

**Table 4:** Design parameters for molten salt storage tank.

| Parameters | Low Temperature Heat Storage Tank |
|---|---|
| Working temperature (°C) | 290 |
| Diameter (m) | 29 |
| Height (m) | 10.5 |
| Tank bottom | Mineral wool, refractory bricks |
| Tank wall | Mineral wool, A516 Gr70 (Carbon steel pressure vessels) |
| Tank top | Mineral wool |

The heat dissipation loss of the low-temperature heat storage tank obtained through simulation is shown in Table 5.

**Table 5:** Heat loss table for heat storage tank.

| | Heat Dissipation Per Unit Area (W·m$^{-2}$) | Heat Loss (kW) | Total Heat Loss (kW) |
|---|---|---|---|
| Tank bottom | 36.95 | 25.5 | |
| Tank wall | 40.37 | 41.9 | 105.7 |
| Tank top | 55.51 | 38.3 | |

As seen in the table, the heat loss of the low-temperature molten salt tank is 105.7 kW, and the total heat loss throughout the day is 2.53 MWh. The heat losses on the top, wall, and bottom of the tank are 25.5, 41.9, and 38.3 kW, respectively. Fig. 10 shows the temperature distribution of the molten salt heat storage tank, and since the bottom of the tank is composed of mineral wool and refractory bricks, which are different from the tank wall and top structure, a significant heat loss occurred.

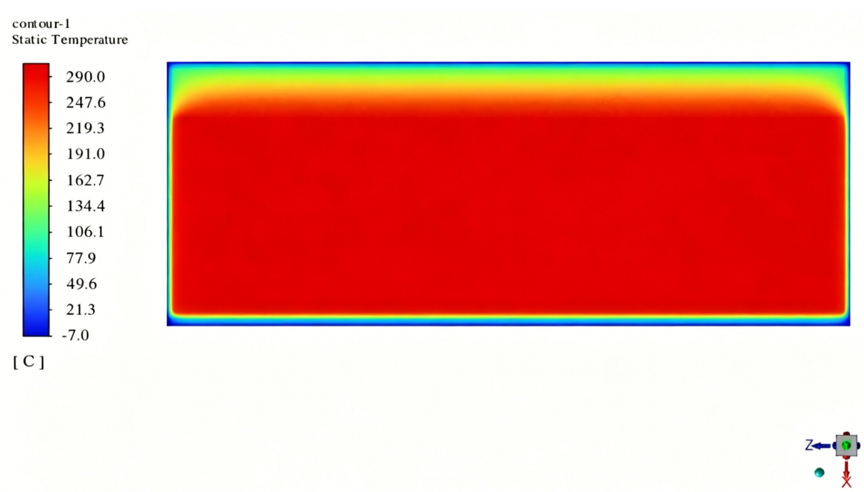


**Figure 10:** Molten salt heat storage tank temperature distribution cloud map.

### *3.3 Economic Analysis of Heat Pump Anti-Condensation System*

The annual operating time of the system is set to 8000 h. The initial investment cost of the anti-condensation system refers to the construction cost of thermal energy storage [18]. The same initial investment cost per kW for coal-fired boilers, gas boilers, and electric tracing can be found in Tan et al., 2022. The annual maintenance cost is set at 2% of the system cost, and the electricity price for heat pumps and electric tracing is based on the industrial electricity price $P_d$ which is 0.85 RMB/kWh.

Initial investment in heat pumps can be expressed as:

$$C_{\mathrm{hp}} = Q_{\mathrm{hp}} \cdot C_{\mathrm{hp}}^{'} \tag{27}$$

$$S_{\mathrm{hp}} = 8000Y \cdot P_d \cdot F \tag{28}$$

where the value of $F$ is 0.8.

### *3.3.1 Coal-Fired Boiler*

The low calorific value of standard coal $Q_{net}$ is 29,307 kJ/kg, with an efficiency of 0.9. The unit price of standard coal, $P_m$, is 800 RMB/t. Then the coal consumption $M$ and fuel costs $S_m$ are equal to

$$M = \frac{Q_0}{\eta_b \times Q_{net}} \tag{29}$$

$$S_m = M \times P_m \tag{30}$$

### *3.3.2 Gas Boilers*

The efficiency of the gas boiler is 0.9, and the price of natural gas is 3.95 RMB/m$^3$. The gas consumption $Q_{con}$ of the gas boiler can be expressed as:

$$Q_{con} = Q_g \times V_{gas} \times 4.18 \tag{31}$$

where $Q_g$ is taken as 8400 kcal/m$^3$.

### *3.3.3 Electric Tracing*

The efficiency of electric tracing is set at 0.97 [19], and the power source for electric tracing usually comes from the power grid or photovoltaic power plants matched with photothermal power plant. The electric tracing is assumed to not produce pollutants [20].

### *3.3.4 Calculation and Comparison of Various Heating Costs*

By comparing the initial investment, annual operating costs, power consumption, and electricity bills of different heating methods, the difference of energy consumption are shown in Table 6.

**Table 6:** Calculation of costs for each heating method (10,000 RMB).

| Heating Method | Electricity Bill | Fuel Cost | Initial Investment | Maintenance Cost |
|---|---|---|---|---|
| Heat pump | 624 | / | 144 | 2.88 |
| Electric tracing | 896 | / | 80 | 1.6 |
| Coal-fired boiler | / | 232 | 40 | 0.8 |
| Gas boiler | / | 815 | 89 | 1.78 |

According to Table 6, although the initial investment of the heat pump system is relatively high, the annual operating cost is slightly lower, and the electrical energy can be obtained from the redundant electricity of the CSP matched photothermal or photovoltaic power generation system, with a slightly lower cost. Furthermore, from the perspective of pollutant emissions, heat pump systems have more advantages.

## 4 Conclusion

In this study, a simulation model is developed to investigate the effects of key parameters on the COP of a heat pump anti-condensation system, including system heat release power, maximum and minimum cycle pressures, heat source temperature, and compressor isentropic efficiency. The model is well validated against experimental data reported in the literature [11]. The results indicate that COP improves with increasing heat release power, whereas a higher maximum cycle pressure reduces the COP. The influence of the minimum cycle pressure on COP exhibits a non-monotonic trend, initially decreasing and then increasing, which is primarily attributed to density variations of supercritical $CO_2$ near the critical point. Furthermore, raising the heat source temperature and enhancing the isentropic efficiency of the compressor are both effective in improving COP [19].

**Acknowledgement:** The authors gratefully acknowledge the financial support from the Postgraduate Scholarship Program of Lanzhou Jiaotong University.

**Funding Statement:** The authors received no specific funding for this study.

**Author Contributions:** Kai Li: Conceptualization, methodology, software, investigation, writing—original draft; Yongheng Zhang: Project administration, funding acquisition, resources, writing—review & editing; Kai Sun: Formal analysis, data curation, software, review & editing; Mingkuan Rong: Engineering data support. All authors reviewed and approved the final version of the manuscript.

**Availability of Data and Materials:** The data utilized in this work are considered proprietary and commercially sensitive, falling under the category of trade secrets protected by applicable laws and regulations. As such, the specific datasets, analysis methodologies, and outcomes detailed in this document cannot be made publicly available or shared beyond the authorized personnel of the organization that owns and maintains these data.

**Ethics Approval:** This study does not involve human participants, animals, or clinical experiments. Therefore, ethical approval is not applicable for this research.

**Conflicts of Interest:** The authors declare no conflicts of interest.

## Nomenclature

### General Symbols

| | |
|---|---|
| $h_{is}$ | Enthalpy under isentropic compression at Node *i* |
| $p_i$ | Pressure at the Node *i* |
| $s_i$ | Entropy of coolant at Node *i* |
| $T_i$ | Compressor inlet temperature of coolant at Node *i* |
| $m_1$ | Coolant fluid mass flowrates at the hot end |
| $m_2$ | Coolant fluid mass flowrates at the cold end |
| $C_{cop}$ | Energy efficiency coefficient |
| $A$ | Surface area of tank |
| $T_{inner}$ | Inner surface temperature of tank |
| $T_a$ | Ambient temperature |
| $T_{outer}$ | Outer surface temperature of tank |
| $Q_1$ | Heat transferred to the top of the heat storage tank |
| $Q_2$ | Heat transferred to upper part of the side wall |

| | |
|---|---|
| $X_{sur,top}$ | Angle coefficient between the molten salt surface and the tank top |
| $r_1$ | Smaller plane circle radius |
| $r_2$ | Larger plane circle radius |
| $d$ | Vertical distance between two circular surfaces |
| $Q_{cv,loss}$ | Convective heat transfer coefficients of molten salt and air |
| $Nu$ | Nusselt number of convective heat transfer |
| $h_c$ | Convective heat transfer coefficient on the bottom surface |
| $Pr$ | Prandtl number |
| $Gr$ | Grashof number |
| $Q_{hp}$, | Energy generated by the heat pump |
| $C_{hp}$ | Cost of the heat pump generating energy |
| $S_{hp}$ | Electricity bill |
| $Y$ | Power of heat pump |
| $F$ | Load factor |
| $P_d$ | Industrial electricity price |
| $Q_0$ | Effective heat utilization in coal-fired boilers |
| $V_{gas}$ | Volume of natural gas |
| $Q_g$ | Calorific value of natural gas |

**Greek Letters**

| | |
|---|---|
| $\eta_s$ | Isentropic efficiency |
| $\eta_m$ | Mechanical efficiency of compressor |
| $\delta$ | Boltzmann constant |
| $\varepsilon$ | Emissivity of surface materials |
| $\eta_b$ | Boiler efficiency |

**Superscript and Subscripts**

| | |
|---|---|
| *sur* | Surface |

## References

1. Koohi-Fayegh S, Rosen MA. A review of energy storage types, applications and recent developments. J Energy Storage. 2020;27(2):101047. doi:10.1016/j.est.2019.101047.
2. Lee D, Jo B. Thermal energy storage characteristics of binary molten salt nanofluids: specific heat and latent heat. Int J Energy Res. 2021;45(2):3231–41. doi:10.1002/er.6019.
3. Kearney D, Kelly B, Herrmann U, Cable R, Pacheco J, Mahoney R, et al. Engineering aspects of a molten salt heat transfer fluid in a trough solar field. Energy. 2004;29(5–6):861–70. doi:10.1016/S0360-5442(03)00191-9.
4. Morandin M, Maréchal F, Mercangöz M, Buchter F. Conceptual design of a thermo-electrical energy storage system based on heat integration of thermodynamic cycles–part A: methodology and base case. Energy. 2012;45(1):375–85. doi:10.1016/j.energy.2012.03.031.
5. Chamoun M, Rulliere R, Haberschill P, Berail JF. Dynamic model of an industrial heat pump using water as refrigerant. Int J Refrig. 2012;35(4):1080–91. doi:10.1016/j.ijrefrig.2011.12.007.
6. Chamoun M, Rulliere R, Haberschill P, Peureux JL. Modelica-based modeling and simulation of a twin screw compressor for heat pump applications. Appl Therm Eng. 2013;58(1–2):479–89. doi:10.1016/j.applthermaleng.2013.04.020.
7. Morandin M, Maréchal F, Mercangöz M, Buchter F. Conceptual design of a thermo-electrical energy storage system based on heat integration of thermodynamic cycles: part B: alternative system configurations. Energy. 2012;45(1):386–96. doi:10.1016/j.energy.2012.03.033.
8. Zhang D, Li B, Zhao Q, Li J. Thermal performance and energy characteristic analysis of multiple renewable energy complementary heat pump system. Sol Energy. 2020;196(16):287–94. doi:10.1016/j.solener.2019.12.030.

9. Li X, Wang Z, Yang M, Yuan G. Dynamic simulation of a novel solar polygeneration system for heat, power and fresh water production based on solar thermal power tower plant. J Therm Sci. 2020;29(2):378–92. doi:10.1007/s11630-020-1163-z.
10. Shaik VB, Tangellapalli S, Kukreja R. Exergy analysis of heat pump polygeneration system. Heat Transf. 2025;54(5):3473–93. doi:10.1002/htj.23367.
11. Salomone-González D, González-Ayala J, Medina A, Roco JMM, Curto-Risso PL, Calvo Hernández A. Pumped heat energy storage with liquid media: thermodynamic assessment by a Brayton-like model. Energy Convers Manag. 2020;226:113540. doi:10.1016/j.enconman.2020.113540.
12. You D, Tatli AE, Metghalchi H. A Brayton pumped thermal energy storage system based on supercritical carbon dioxide recompression reheating discharge cycle. ASME Open J Eng. 2025;4(6):041002. doi:10.1115/1.4067446.
13. Wan Z, Wei J, Qaisrani MA, Fang J, Tu N. Evaluation on thermal and mechanical performance of the hot tank in the two-tank molten salt heat storage system. Appl Therm Eng. 2020;167(12):114775. doi:10.1016/j.applthermaleng.2019.114775.
14. Davis D, Jafarian M, Chinnici A, Saw WL, Nathan GJ. Thermal performance of Vortex-based solar particle receivers for sensible heating. Sol Energy. 2019;177(4):163–77. doi:10.1016/j.solener.2018.10.086.
15. Pacheco JE. Final test and evaluation results from solar two project. Livermore, CA, USA: Sandia National Laboratories; 2002. doi:10.2172/793226.
16. Liu Y, Wang X, Zhang L. Thermo-economic examination of ocean heat-assisted pumped thermal energy storage system using transcritical $CO_2$ cycles. Appl Therm Eng. 2024;255(11):123992. doi:10.1016/j.applthermaleng.2024.123992.
17. Ayachi F, Tauveron N, Tartière T, Colasson S, Nguyen D. Thermo-electric energy storage involving $CO_2$ transcritical cycles and ground heat storage. Appl Therm Eng. 2016;108(5):1418–28. doi:10.1016/j.applthermaleng.2016.07.063.
18. Vinnemeier P, Wirsum M, Malpiece D, Bove R. Integration of heat pumps into thermal plants for creation of large-scale electricity storage capacities. Appl Energy. 2016;184(1):506–22. doi:10.1016/j.apenergy.2016.10.045.
19. Boretti A. Optimizing concentrated solar power: high-temperature molten salt thermal energy storage for enhanced efficiency. Energy Storage. 2024;6(7):e70059. doi:10.1002/est2.70059.
20. Chen J, Li S, Zhang Y. Thermodynamic analysis of a transcritical $CO_2$ heat pump for heating applications. Energy. 2025;321(1):134896. doi:10.1016/j.energy.2025.134896.